



# Ultrafast convergent power-balance model for Raman random fiber laser with half-open cavity

SHENGTAO LIN,<sup>1</sup> ZINAN WANG,<sup>1,\*</sup>  HUGO A. ARAÚJO,<sup>2</sup> ERNESTO P. RAPOSO,<sup>2,3,4</sup> ANDERSON S. L. GOMES,<sup>5</sup> HAN WU,<sup>6</sup>  MENGQIU FAN,<sup>7</sup> AND YUNJIANG RAO<sup>1</sup>

<sup>1</sup>Key Laboratory of Optical Fiber Sensing and Communications, University of Electronic Science and Technology of China, Chengdu 611731, China

<sup>2</sup>Laboratório de Física Teórica e Computacional, Departamento de Física, Universidade Federal de Pernambuco, Recife 50670-901, Brazil

<sup>3</sup>Centre d'Estudis Avançats de Blanes-CEAB-CSIC, 17300, Girona, Spain

<sup>4</sup>Centre for Ecological Research, and Forestry Applications-CREAF, Universitat Autònoma de Barcelona, 08193, Cerdanyola del Vallès, Spain

<sup>5</sup>Departamento de Física, Universidade Federal de Pernambuco, 50670-901, Recife, PE, Brazil

<sup>6</sup>College of Electronics and Information Engineering, Sichuan University, Chengdu, Sichuan 610064, China

<sup>7</sup>Research Center of Laser Fusion, China Academy of Engineering Physic, Mianyang 621900, China

\*znwang@uestc.edu.cn

**Abstract:** The power-relevant features of Raman random fiber laser (RRFL), such as lasing threshold, slope efficiency, and power distribution, are among the most critical parameters to characterize its operation status. In this work, focusing on the power features of the half-open cavity RRFL, an ultrafast convergent power-balance model is proposed, which highlights the physical essence of the most common RRFL type and sharply reduces the computation workload. By transforming the time-consuming serial calculation to a parallel one, the calculation efficiency can be improved by more than 100 times. Particularly, for different point-mirror reflectivities and different fiber lengths, the input-output power curves and power distribution curves calculated by the present model match nicely with those of the conventional model, as well as with the experimental data. Moreover, through the present model the relationship between point-mirror reflectivity and laser threshold is analytically derived, and the way for improving RRFL's slope efficiency is also provided with a lucid theoretical explanation.

© 2020 Optical Society of America under the terms of the [OSA Open Access Publishing Agreement](#)

## 1. Introduction

Raman random fiber laser (RRFL) combines the features of nano-particle based random lasers [1] with easy fabrication and simple configuration, and those of conventional Raman fiber lasers with wavelength agility [2,3] and high efficiency [4–6], attracting extensive attention in recent years [7–10]. RRFL was first proposed in 2010 by using a long telecommunication fiber [11], which naturally shows advantages in the field of long-distance distributed amplification [12,13], and remotely point sensing [14,15].

To reveal its inherent lasing mechanism, various RRFL mathematical models were established. The power-balance model can be used to characterize the power features including lasing threshold, slope efficiency, power distribution [4,11], and high-order emission profiles [16]. The modified power-balance model [17] described the spectral properties, and the nonlinear Schrödinger equation based model [18] can further study the spectral and temporal intensity dynamics of RRFL. Besides, wave kinetic theory [19] can be also used to study the spectral and power properties of RRFL. However, as these models of RRFL are becoming more and more sophisticated, it takes more and more computational load to generate numerical results, which could be quite inconvenient in most practical applications that take power properties as priority.

For the distributed amplification, the power distribution is the focus of consideration, and for point-sensing system it could be the threshold. In fact, a model that can quickly calculate these features in a half-open cavity RRFL is highly desired for most applications [20,21], as it would help to the system designer to grip the major outcome without going through all the details. The first analytical RRFL model with formulas describing power features was proposed in Ref. [22] and improved in Ref. [23], which has been well applied in the forward-pumped long cavity structure. In 2016, a "minimalist" power-balance model for forward-pumped RRFL with 100% reflectivity was proposed [24], which has no strict requirements on fiber length. However, to the best of our knowledge, there is not any computationally optimized model for the backward-pumped RRFL or forward-pumped RRFL with arbitrary reflective mirror.

In this work, an ultrafast convergent power-balance model for half-open cavity RRFL is presented, which manifests the critical lasing mechanism and largely decreases the computational workload. Based on the present model, it becomes apparent how Rayleigh scattering coefficient and fiber length would change the slope efficiency. In addition, the dependence of the lasing threshold over point-mirror reflectivity is analytically derived, in nice agreement with the numerical simulations and experimental data. Therefore, it can be widely used for most cases of half-open cavity RRFL.

## 2. Modification of the conventional power-balance model

The well-known power-balance model [11,25] is used as the starting point for our approach. Half-open cavity means there is a point-mirror, e.g., a fiber Bragg grating, at one side of the cavity. The pump and Stokes lightwaves transmitted in the opposite directions can be ignored in the proposed model. In addition, the random distributed Rayleigh backscattering is considered as an equivalent point-mirror. As it could be seen at the end of the deduction, this model is similar to the conventional Raman fiber lasers model [26], and can be used to easily explain some of the major features of half-open cavity RRFL.

The power-balance model considers Raman nonlinear amplification, fiber linear loss and Rayleigh scattering in different propagation directions. It has been proved to describe the power features of RRFL very well [11,23], and can be expressed as:

$$\frac{dP_p^\pm}{dx} \pm \alpha_p P_p^\pm = \mp \left( \frac{\nu_p}{\nu_s} \right) g_R P_p^\pm (P_s^+ + P_s^-) \pm \varepsilon_p P_p^\mp, \quad (1)$$

$$\pm \frac{dP_s^\pm}{dx} + \alpha_s P_s^\pm = g_R P_s^\pm (P_p^+ + P_p^-) + \varepsilon_s P_s^\mp, \quad (2)$$

where  $P$  denotes the optical power; lower indexes 'p' and 's' correspond to the pump and the Stokes lasing, respectively; '+' and '-' denotes the forward and backward waves in the direction, respectively;  $\nu$  is the wave frequency;  $\alpha$  is the fiber linear loss;  $g_R$  is the Raman gain index;  $\varepsilon$  is the Rayleigh backscattering coefficient.

To obtain the solution of Eqs. (1) and (2), four boundary conditions are needed. The pump power ( $P_{in}$ ) is launched into the fiber at the position  $x = 0$ , thus  $P_p(0) = P_{in}$ . In addition,  $P_p^+(0) = R_{Lp} P_p^-(0)$ ,  $P_s^+(0) = R_{Ls} P_s^-(0)$  and  $P_s^-(L) = R_{Rs} P_s^+(L)$ , where  $R_{Lp}$ ,  $R_{Ls}$  and  $R_{Rs}$  are the pump wave reflectivity at the left fiber end, Stokes wave reflectivity at the left and right fiber end, respectively. Taking the backward-pumped cavity RRFL as an example, we notice that  $R_{Rs}$  depends on the reflectivity of the mirror;  $R_{Ls}$  is the parasitic reflection.

Based on this model, the resonator of the half-open RRFL consists of two mirrors, that is, a traditional point-mirror such as FBG or fiber loop mirror, and the distributed mirror composed of random distributed feedback from Rayleigh backscattering. Here, a simplification is performed, and the special mirror can be considered as a point-mirror placed at the fiber end with similar effects. Under this assumption, RRFL essentially becomes a conventional Raman fiber laser, as shown in Fig. 1.

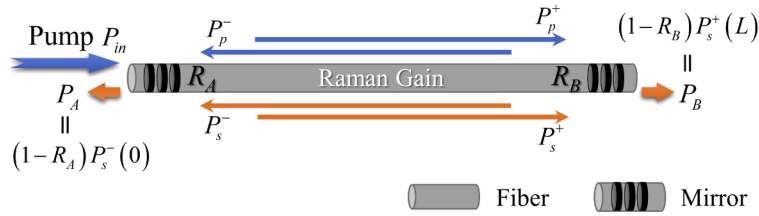


Fig. 1. The schematic diagram of the simplified RRFL.

For the conventional oscillator and above the threshold, the forward propagating power and backward propagating power has the following relationship [27]:

$$P_s^-(0)P_s^+(0) = P_s^+(x)P_s^-(x) = P_s^+(L)P_s^-(L). \quad (3)$$

Moreover, assuming that the reflectivity of the two RRFL mirrors are \$R\_A\$ and \$R\_B\$, the boundary condition for Stokes lasing can be rewritten as: \$\sqrt{R\_A}P\_s^-(0) = \sqrt{R\_B}P\_s^+(L)\$. Thus, the ratio of laser powers coupled out from both sides of the fiber end can be expressed as [26]:

$$\frac{P_A}{P_B} = \frac{1 - R_A}{1 - R_B} \sqrt{\frac{R_B}{R_A}}. \quad (4)$$

Therefore, if there is a mirror with extremely low reflectivity that satisfies \$R\_A \gg R\_B\$ or \$R\_B \gg R\_A\$, such as the distributed mirror in RRFL, the laser will be mainly output from one end of the fiber with high efficiency, even reaching the quantum limit [4]. It is worth noting that the optical slope efficiency of the half-open cavity RRFL is related to the fiber length and Rayleigh scattering coefficients. As the cavity length (fiber length) becomes longer or has a higher Rayleigh scattering coefficient, the cumulative distributed feedback from Rayleigh backscattering becomes more significant, which results in an increase in the reflectivity of the equivalent point-mirror. According to Eq. (4), a reduction in the reflectivity difference between the two mirrors will lead to a decrease in the slope of efficiency.

To further reduce the amount of computation, some approximations are used. First, the Rayleigh scattering wave \$P\_p^-\$ is thousands of times lower than the forward pump power \$P\_p^+\$ in conventional fibers, so its effect on the forward pump power and Stokes powers can be ignored [17,23,24]. Moreover, the power generated by the Rayleigh scattering reflection is also much smaller than that of the point-mirror reflection. Thus, based on Eq. (3) for the forward-pumped RRFL, the forward-propagating Stokes lasing is much higher than the backward one, and \$P\_s^-\$ can be also neglected [24] in Eq. (1) and (2). Further, for the backward-pumped RRFL, the backward-propagating Stokes lasing is higher than the forward one, and \$P\_s^+\$ can be neglected as well.

Combining all above approximations, the steady-state Eqs. (1) and (2) for backward-pumped RRFL can be simplified into two equations:

$$\frac{dP_p^+}{dx} + \alpha_p P_p^+ = -\frac{1}{v_s} g P_p^+ P_s^-, \quad (5)$$

$$-\frac{dP_s^-}{dx} + \alpha_s P_s^- = \frac{1}{v_p} g P_s^- P_p^+, \quad (6)$$

where \$g \equiv v\_p g\_R\$ for the symmetry and aesthetics of the equations. Besides, only two boundary conditions are required:

$$P_p^+(0) = P_{in}, \quad (7)$$

$$P_s^-(L) = \sqrt{R_{eff}} \sqrt{R} P_s^-(0), \quad (8)$$

where  $R$  is the reflectivity of the traditional point-mirror and  $R_{eff}$  is the reflectivity of the equivalent point-mirror. For the forward-pumped RRFL, the steady-state Eq. (6) and boundary condition (8) should be changed to:

$$\frac{dP_s^+}{dx} + \alpha_s P_s^+ = \frac{1}{v_p} g P_s^+ P_p^+, \quad (9)$$

$$P_s^+(0) = \sqrt{R_{eff}} \sqrt{R} P_s^+(L). \quad (10)$$

It should be noted that, for the half-open cavity RRFL, the value of  $R_{eff}$  is directly related to the Rayleigh scattering coefficient, and the increase of the coefficient will reduce the threshold ( $P_{th}$ ) of RRFL. Thus, the relationship between  $R_{eff}$  and  $P_{th}$  is inversely proportional, which can be expressed as (similar to [28]):

$$\sqrt{R_{eff}} = \frac{1}{\sqrt{R}} \exp(-g_R P_{th} L_{eff} + \alpha_s L), \quad (11)$$

where  $L_{eff}$  is the effective fiber length ( $L_{eff} \equiv \frac{1}{\alpha} [1 - \exp(-\alpha L)]$ ). For a certain length of fiber, the value of  $R_{eff}$  is a constant, and the threshold power can be written as a function of the point-mirror reflectivity:

$$P_{th}(R) = -\frac{1}{G} \ln(R) + \kappa, \quad (12)$$

where  $G = 2g_R L_{eff}$  and  $\kappa = [\alpha_s L - 0.5 \ln(R_{eff})] / g_R L_{eff}$ . Thus, the threshold of RRFL decreases logarithmically with the increasing mirror reflectivity. This equation clearly explains why the threshold of the half-open RRFL is much lower than that of the open cavity RRFL.

### 3. Solution for the ultrafast convergent power-balance model

In order to quickly obtain solutions of the ultrafast convergent power-balance model (UCM), a novel solving procedure is proposed. Since the model is applicable to both the forward and backward pumped structures and the iterative process is similar, the backward-pumped RRFL is used as an example to illustrate the process.

Integrating the Eqs. (5) and (6) over the range 0 to  $x$  gives:

$$P_p^+(x) = P_p^+(0) e^{-\alpha_p x} \exp\left[-\frac{g}{v_s} \int_0^x P_s^-(x) dx\right], \quad (13)$$

$$P_s^-(x) = P_s^-(0) e^{\alpha_s x} \exp\left(-\frac{g}{v_p} \int_0^x P_p^+(x) dx\right), \quad (14)$$

which can be used to iteratively obtain accurate power distribution curves. The first part of the index term ( $\alpha x$ ) in those two equations represents the fiber linear loss, and the second index term represents the nonlinear cumulative power transfer of the Raman effect. Furthermore, the correct value of  $P_s^-(0)$  is also satisfied with the boundary condition (8), and substituting it into Eq. (14) one can obtain a critical relation:

$$\sqrt{R_{eff}} \sqrt{R} = e^{\alpha_s L} \exp\left(-\frac{g}{v_p} \int_0^L P_p^+(x) dx\right). \quad (15)$$

Thus, the value of  $P_s^-(0)$  for each pump power can be selected by the shooting method based on Eq. (15). It should be further noted that, no matter how the values of  $P_p^+(0)$  changes, the integral result of  $P_p^+(x)$  is always a constant (i.e.,  $\int_0^L P_p^+(x) dx = \text{constant}$ ), which is the same for

the forward-pumped case. In other words, the excess pump energy  $P_{in}$  will be transferred to the Stokes wave, and the integral power for the Stokes wave goes up with the increase of the pump power.

Based on the Eqs. (13)–(15), the iterative block diagram for solving Eqs. (5) and (6) is shown in Fig. 2, which includes two loop bodies: "loop body one" is to obtain accuracy power distributions using given boundary conditions, and "loop body two" is to find the correct boundary conditions that satisfy Eq. (15). The specific process is as follows:

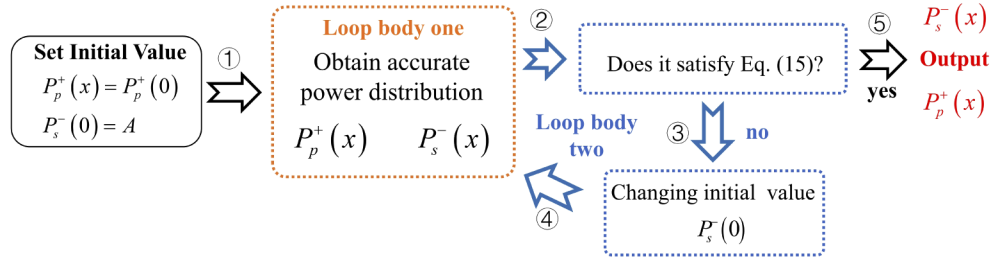


**Fig. 2.** The iterative block diagram for solving Eqs. (5) and (6).

①: Set the initial values of  $P_p^+(x)$  and  $P_s^-(0)$  to  $P_p^+(0)$  and  $A$ , respectively, and the value of  $A$  can be arbitrarily selected from 0 to  $P_p^+(0)$ . At the time  $T_0$ , send them into "loop body one" shown in Fig. 3(b), at which time the power distribution of  $P_p^+(x)$  is uniform. Then at time  $T_1$ , substitute the distribution of  $P_p^+(x)$  into Eq. (14) to obtain a preliminary expression for  $P_s^-(x)$ :

$$P_s^-(x) = P_s^-(0) e^{\alpha_s x} \exp\left(-\frac{g}{\nu_p} P_p^+(0) x\right). \quad (16)$$

At time  $T_2$ , integrate the expression  $P_s^-(x)$  to get  $P_p^+(x)$ :

$$P_p^+(x) = P_p^+(0) \exp\left\{-\alpha_p x - \frac{g \nu_p P_s^-(0)}{\nu_s [\alpha_s \nu_p - g P_p^+(0)]} \left[e^{\left(\alpha_s - \frac{g}{\nu_p} P_p^+(0)\right) x} - 1\right]\right\}. \quad (17)$$

It should be noted that Eq. (17) can already be considered as the final analytic solution of  $P_p^+(x)$ , because it is close enough to the final values, as shown in Fig. 4. The final expression of  $P_s^-(x)$  can be also obtained after substituting Eq. (17) into Eq. (14) at time  $T_3$ . In addition, the accuracy of the calculated power distributions  $P_p^+(x)$  and  $P_s^-(x)$  can be further improved after repeatedly executing the process from  $T_1$  to  $T_2$  to  $T_3$ .

②: If the output result  $P_p^+(x)$  do not meet the condition (15), then go to step ③, otherwise to step ⑤.

③: Change the initial value of  $P_s^-(0)$ : if the integration result of  $P_p^+(x)$  is too large, increase the initial value  $P_s^-(0)$ ; otherwise, decrease its value.

④: Calculate the power distributions  $P_p^+(x)$  and  $P_s^-(x)$  again based on the renewed boundary conditions.

⑤: Obtain the final power distributions of  $P_p^+(x)$  and  $P_s^-(x)$ .

Moreover, the iterative process described above can be also used for the forward-pumped structure, requiring only a few modifications in Eq. (14):

$$P_s^+(x) = P_s^+(0) e^{-\alpha_s x} \exp\left(\frac{g}{\nu_p} \int_0^x P_p^+(x) dx\right). \quad (18)$$

For the "loop body one", it is a time-saving and accurate process compared to traditional Euler method for numerically solving differential equations. Using the present model, the

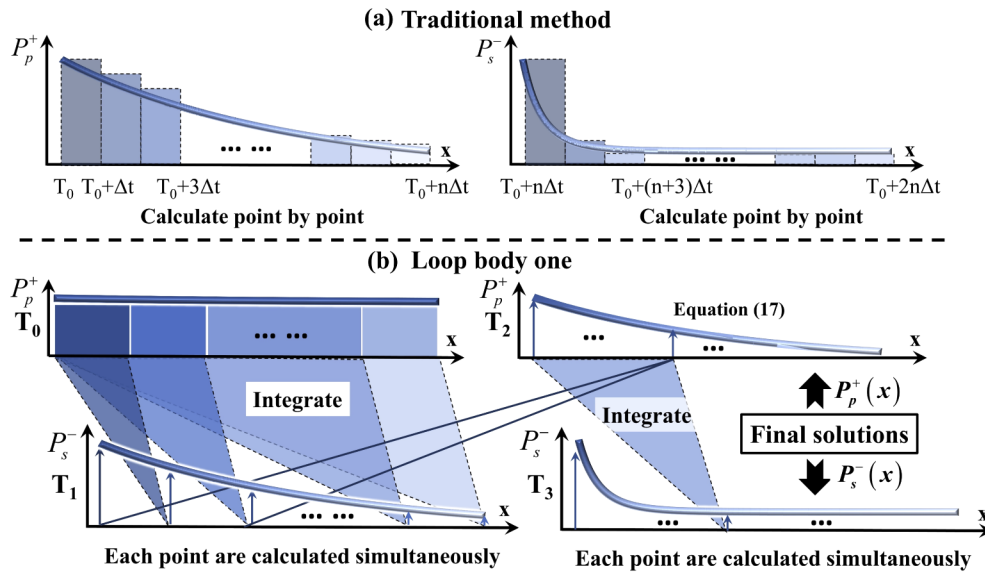


**Fig. 3.** Methods for solving the systems of differential equations of the RRFL: (a) traditional Euler method; (b) the method for solving UCM used in "loop body one".

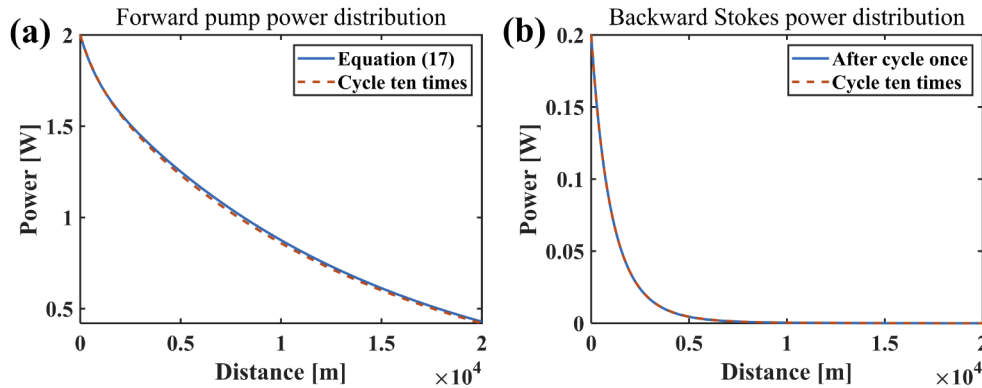


**Fig. 4.** The power distribution for (a) forward pump wave; (b) backward Stokes wave under 20 km backward-pumped structure with initial value  $P_p^+(0) = 2$  W and  $P_s^-(0) = 0.2$  W. After cycle once: Time  $T_3$  in Fig. 3(b).

power distribution of  $P_p^+(x)$  can be directly calculated by Eq. (17). Although calculating the  $P_s^-(x)$  involves numerical integration through Eq. (14), the power of each point can be obtained simultaneously by parallel calculation, as shown in Fig. 3(b), which is beneficial to introduce the GPU acceleration in the calculation and achieve ultrafast convergence. Even if the "loop body one" is executed multiple times for improving accuracy, the calculation speed will be much faster than the traditional method that needs to calculate millions of power values point by point, as shown in Fig. 3(a).

For the "loop body two", it is a memory-saving and easy-execute process compared to the iteration of the conventional model based on Eq. (1) and (2). Using our present model, the number of differential equations is reduced from 4 to 2, which saves nearly half of the computer memory. In addition, the boundary conditions are also greatly reduced, and the value of  $P_s^-(0)$  can be obtained only through a simple iteration, while for conventional model three boundary values

(i.e.,  $P_p^-(0)$ ,  $P_s^-(0)$  and  $P_s^+(0)$ ) need to be determined simultaneously, which largely increases the iterative difficulty and time consumption.

Due to the above factors, the calculate speed of the UCM could be more than 100 times faster than that of the conventional model, and it could be much higher with a computation platform with more threads, such as using better performance GPU or distributed computation. The simulation comparison is set as follows: divide the fiber into 500,000 elements, and calculate 50-point pump power. For the present model, as the "loop body one" circulates 5 times and "loop body two" executes 200 times using GPU with 896 CUDA cores, the average calculation duration is only 71.4 seconds (about 1.2 minutes), while the conventional model requires 7967 seconds (more than 2 hours).

#### 4. Validation of UCM with experimental and simulation results

We have also performed experiments and numerical simulation in order to verify the correctness of the UCM. For the experimental part, we apply the UCM to some typical RRFL structures, and compare them with the results of conventional model and experiments to illustrate its accuracy and reliability. For the numerical simulation, the conventional model is also used for comparison, which has been proved to provide results close to the experimental ones. We show in the simulation part the power properties of different point reflectivities and different fiber lengths, respectively.

Some typical experiments are carried out to verify whether the solution of the UCM is closed to the actual values. The measured output Stokes power versus pump power is shown in Fig. 5. Besides, the dotted lines correspond to the calculated output power based on the conventional model, while the dots correspond to the calculated output power based on the UCM.

For the backward-pumped experiments, we apply the present model to the low-threshold and high-efficiency RRFL with a 60% reflectivity fiber loop mirror [29]. The pump wavelength is set as 1090 nm, the corresponding 1st-order Stokes is 1145 nm, and the laser cavity uses 5 km standard single-mode fiber (SMF). From the results on the right side of Fig. 5, even at high pump power ( $\sim 10$  W) and using relatively short cavity, those two models are in good agreement and both fit the experimental data well.

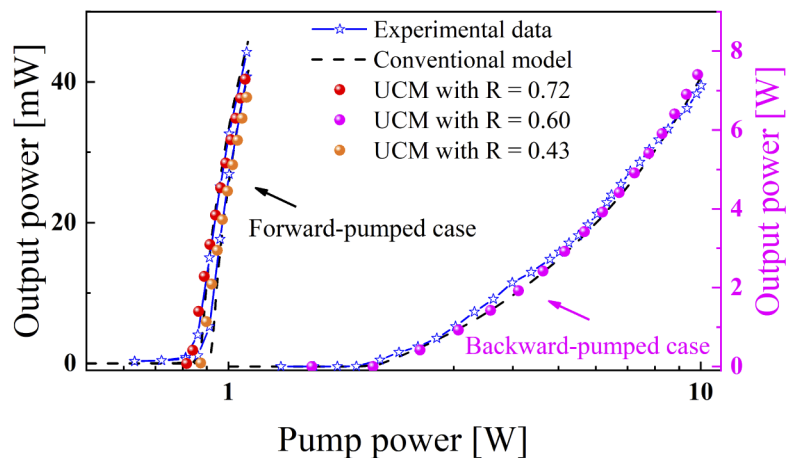


**Fig. 5.** Output power vs. pump power for some typical half-open cavity RRFL structure. UCM: ultrafast convergent power-balance model.

For the forward-pumped experiments, two point-mirrors with 72% reflectivity and 43% reflectivity are analyzed [30], respectively. In this case, a 1365 nm Raman fiber laser is used

as the pump laser to generate the 1455 nm 1st-order Stokes laser in the 50 km SMF. The results calculated by those two models also fit the experimental data well, which is shown in the left side of Fig. 5. In addition, as the mirror reflectivity decreases from 72% to 43%, the laser threshold is increased about 0.04 W, which is consistent with the theoretical result  $\ln \left[ (0.72/0.43) / 2g_R L_{eff} \right] \approx 0.041$  W calculated according Eq. (12). Thus, the present model can be used to reflect the actual power properties well, and simulation results of the conventional model can be also used as a standard reference for further testing the accuracy of the present model.

The simulation part gives a more detailed display of the power properties and further discusses the results of Eqs. (4) and (12). The simulated laser structure is described as follows: pump wavelength 1365 nm; Raman laser wavelength 1455 nm; a 1455 nm FBG is placed at one port of the fiber end and the other parameters are summarized in Table 1.

**Table 1. Parameters for the numerical calculation**

Wavelength (nm)	$\alpha$ (dB/km)	$\varepsilon$ ( $km^{-1}$ )	$g_R$ ( $W^{-1}km^{-1}$ )
1365	0.31	$1 \times 10^{-4}$	0.53
1455	0.24	$6 \times 10^{-5}$	-

To study the effect of the point-mirror reflectivity on the RRFL, the fiber length is fixed at 10 km. The simulation results for backward-pumped RRFL are shown in Figs. 6(a)-(c), and Figs. 6(d)-(f) are the results of the forward-pumped RRFL. Figures 6(a) and 6(d) show the output power of the Raman random lasing power versus pump power with reflectivity 99%, 50% and 25%. The solution of present model matches nicely with the results from the conventional model. Figures 6(b) and 6(e) display the power distribution with 25%-point reflectiveness at 2 W pump power. The results of backward-pumped structure are much close to those of the conventional method. However, for the forward-pumped RRFL the deviation is a bit enlarged. This is caused by the larger output Stokes power in this case, which is more likely to transferring the energy to the opposite direction. Overall, the deviation is rather small especially at the output port, indicating that the assumptions used in the simplification process are plausible. Figures 6(c) and 6(f) reflect the change of the laser threshold with the point-mirror reflectivity. Regardless if it concerns the forward or backward pump structure, the change trend is consistent with Eq. (12).

To study the effect of the fiber length on the UCM of RRFL, the mirror reflectivity is fixed at 99% and the results are shown in Fig. 7. For the backward-pumped case in Fig. 7(a), the output Stokes power is shown to be close to result of the conventional model within the 50 km fiber. With further increase of fiber length, the structure of backward-pumped fiber cavity tends to be a full-open cavity and the present model used in this case will naturally yield less accurate results. However, this does not occur with the forward-pumped structure shown in Fig. 7(b). Moreover, it can be also observed that regardless of the forward or backward pumped structure, the slope efficiency decreases with the increase of the fiber length, which is consistent with the inference of Eq. (4). The equation lucidly shows that reducing the Rayleigh scattering coefficient or decreasing fiber length of the RRFL can improve the optical-optical conversion efficiency, while the traditional model could reach the same conclusion but in an indirect way (e.g., by calculating the efficiency v.s. length curve).

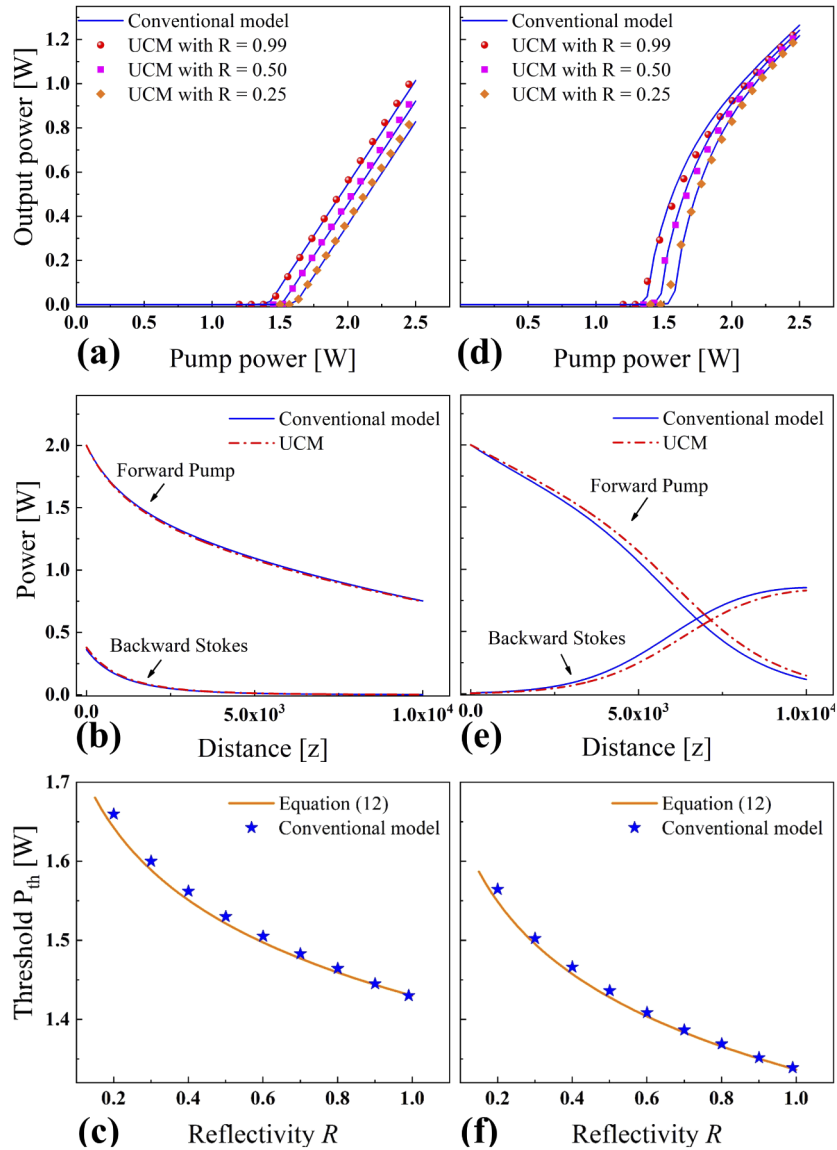


**Fig. 6.** Comparison between the conventional model and the UCM for the half-open cavity RRFL. (a-c) backward-pumped RRFL; (d-f) forward-pumped RRFL. (a) and (d) Raman output power vs. pump power with different reflectivity values; (b) and (e) power distribution with 25% reflective mirror at 2 W pump power; (c) and (f) the threshold of RRFL as a function of point-mirror reflectivity.

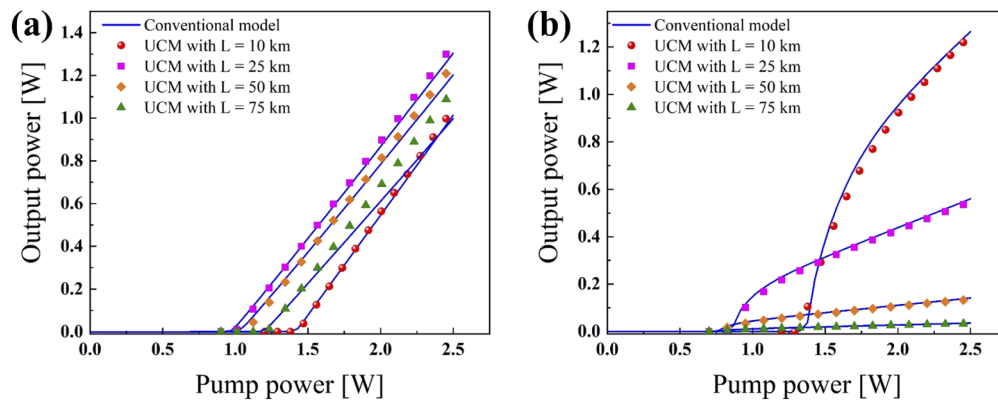


**Fig. 7.** Comparison between the conventional model and the UCM with different fiber length: (a) backward-pumped RRFL; (b) forward-pumped RRFL.

## 5. Conclusion

An ultrafast convergent power-balance model for half-open cavity RRFL is proposed, where the essential relations between the key parameters become much more transparent and intuitive, e.g., the ways for enhancing the slope efficiency, as well as the relationship between the lasing threshold and the point-mirror reflectivity. Meanwhile, the model can significantly reduce the computation load and speed up the calculation procedure (a factor of  $>100$  times acceleration has been demonstrated). We thus hope that the model and the corresponding solving procedures can help to provide a very efficient platform for designing optical sources, distributed amplifiers and sensing systems based on half-open cavity RRFL.

## Funding

National Natural Science Foundation of China (61635005, 61731006); Sichuan Provincial Project for Outstanding Young Science and Technology Scholars (2020JDJQ0024); 111 project (B14039); Conselho Nacional de Desenvolvimento Científico e Tecnológico; Coordenação de Aperfeiçoamento de Pessoal de Nível Superior; Fundação de Amparo à Ciência e Tecnologia do Estado de Pernambuco (APQ-0602-1.05/14, Grant 465.763/2014-6).

## Disclosures

The authors declare no conflicts of interest.

## References

1. F. Luan, B. Gu, A. S. Gomes, K.-T. Yong, S. Wen, and P. N. Prasad, "Lasing in nanocomposite random media," *Nano Today* **10**(2), 168–192 (2015).
2. L. Zhang, H. Jiang, X. Yang, W. Pan, and Y. Feng, "Ultra-wide wavelength tuning of a cascaded Raman random fiber laser," *Opt. Lett.* **41**(2), 215 (2016).
3. J. Dong, L. Zhang, H. Jiang, X. Yang, W. Pan, S. Cui, X. Gu, and Y. Feng, "High order cascaded Raman random fiber laser with high spectral purity," *Opt. Express* **26**(5), 5275 (2018).
4. Z. Wang, H. Wu, M. Fan, L. Zhang, Y. Rao, W. Zhang, and X. Jia, "High Power Random Fiber Laser With Short Cavity Length: Theoretical and Experimental Investigations," *IEEE J. Sel. Top. Quantum Electron.* **21**(1), 10–15 (2015).
5. J. Xu, L. Huang, M. Jiang, J. Ye, P. Ma, J. Leng, J. Wu, H. Zhang, and P. Zhou, "Near-diffraction-limited linearly polarized narrow-linewidth random fiber laser with record kilowatt output," *Photonics Res.* **5**(4), 350 (2017).
6. J. Xu, L. Huang, J. Ye, J. Wu, H. Zhang, H. Xiao, J. Leng, and P. Zhou, "Power scalability of a linearly-polarized narrowband random fiber laser in an all-fiber MOPA structure with 0.1 nm linewidth," *Laser Phys. Lett.* **14**(9), 095101 (2017).

7. H. Wu, B. Han, Z. Wang, G. Genty, G. Feng, and H. Liang, "Temporal ghost imaging with random fiber lasers," *Opt. Express* **28**(7), 9957 (2020).
8. D. V. Churkin, S. Sugavanam, I. D. Vatnik, Z. Wang, E. V. Podivilov, S. A. Babin, Y. Rao, and S. K. Turitsyn, "Recent advances in fundamentals and applications of random fiber lasers," *Adv. Opt. Photonics* **7**(3), 516 (2015).
9. J. Xu, J. Ye, P. Zhou, J. Leng, H. Xiao, H. Zhang, J. Wu, and J. Chen, "Tandem pumping architecture enabled high power random fiber laser with near-diffraction-limited beam quality," *Sci. China: Technol. Sci.* **62**(1), 80–86 (2019).
10. J. Xu, J. Wu, J. Ye, J. Song, B. Yao, H. Zhang, J. Leng, W. Zhang, P. Zhou, and Y. Rao, "Optical rogue wave in random fiber laser," *Photonics Res.* **8**(1), 1 (2020).
11. S. K. Turitsyn, S. A. Babin, A. E. El-Taher, P. Harper, D. V. Churkin, S. I. Kablukov, J. D. Ania-Castañón, V. Karalekas, and E. V. Podivilov, "Random distributed feedback fibre laser," *Nat. Photonics* **4**(4), 231–235 (2010).
12. X. Jia, Y. Rao, F. Peng, Z. Wang, W. Zhang, H. Wu, and Y. Jiang, "Random-lasing-based distributed fiber-optic amplification," *Opt. Express* **21**(5), 6572 (2013).
13. Y. Fu, Z. Wang, R. Zhu, N. Xue, J. Jiang, C. Lu, B. Zhang, L. Yang, D. Atubga, and Y. Rao, "Ultra-long-distance hybrid BOTDA/ $\Phi$ -OTDR," *Sensors* **18**(4), 976 (2018).
14. Z. N. Wang, Y. J. Rao, H. Wu, P. Y. Li, Y. Jiang, X. H. Jia, and W. L. Zhang, "Long-distance fiber-optic point-sensing systems based on random fiber lasers," *Opt. Express* **20**(16), 17695 (2012).
15. M. Fernandez-Vallejo, M. Bravo, and M. Lopez-Amo, "Ultra-long laser systems for remote fiber Bragg gratings arrays interrogation," *IEEE Photonics Technol. Lett.* **25**(14), 1362–1364 (2013).
16. Z. Wang, H. Wu, M. Fan, Y. Rao, X. Jia, and W. Zhang, "Third-order random lasing via Raman gain and Rayleigh feedback within a half-open cavity," *Opt. Express* **21**(17), 20090 (2013).
17. I. D. Vatnik and D. V. Churkin, "Modeling of the spectrum in a random distributed feedback fiber laser within the power balance modes," in *Laser Sources and Applications II*, vol. 9135 J. I. Mackenzie, H. Jelínková, T. Taira, and M. Abdou Ahmed, eds. (2014), p. 91351Z.
18. S. V. Smirnov and D. V. Churkin, "Modeling of spectral and statistical properties of a random distributed feedback fiber laser," *Opt. Express* **21**(18), 21236 (2013).
19. I. V. Kolokolov, D. V. Churkin, I. D. Vatnik, E. V. Podivilov, I. S. Terekhov, S. K. Turitsyn, S. S. Vergeles, V. V. Lebedev, S. A. Babin, M. A. Nikulin, and G. Falkovich, "Wave kinetics of random fibre lasers," *Nat. Commun.* **6**(1), 6214 (2015).
20. V. de Miguel Soto and M. López-Amo, "Truly remote fiber optic sensor networks," *JPhys Photonics* **1**(4), 042002 (2019).
21. X. Du, H. Zhang, H. Xiao, P. Ma, X. Wang, P. Zhou, and Z. Liu, "High-power random distributed feedback fiber laser: From science to application," *Ann. Phys.* **528**(9-10), 649–662 (2016).
22. S. A. Babin, A. E. El-Taher, P. Harper, E. V. Podivilov, and S. K. Turitsyn, "Tunable random fiber laser," *Phys. Rev. A* **84**(2), 021805 (2011).
23. D. V. Churkin, A. E. El-Taher, I. D. Vatnik, J. D. Ania-Castañón, P. Harper, E. V. Podivilov, S. A. Babin, and S. K. Turitsyn, "Experimental and theoretical study of longitudinal power distribution in a random DFB fiber laser," *Opt. Express* **20**(10), 11178 (2012).
24. S. A. Babin, E. A. Zlobina, S. I. Kablukov, and E. V. Podivilov, "High-order random Raman lasing in a PM fiber with ultimate efficiency and narrow bandwidth," *Sci. Rep.* **6**(1), 22625 (2016).
25. D. V. Churkin, S. A. Babin, A. E. El-Taher, P. Harper, S. I. Kablukov, V. Karalekas, J. D. Ania-Castañón, E. V. Podivilov, and S. K. Turitsyn, "Raman fiber lasers with a random distributed feedback based on Rayleigh scattering," *Phys. Rev. A* **82**(3), 033828 (2010).
26. Y. Feng, L. R. Taylor, and D. B. Calia, "150 W highly-efficient Raman fiber laser," *Opt. Express* **17**(26), 23678 (2009).
27. X. Hu, T. Ning, L. Pei, Q. Chen, J. Li, J. Zheng, and C. Zhang, "Shooting method with excellent initial guess functions for multipoint pumping  $Yb^{3+}$ -doped fiber lasers," *Opt. Commun.* **336**, 286–294 (2015).
28. G. P. Agrawal, *Nonlinear fiber optics* (Academic Press, 2006), 4th ed., Chap. 8, pp. 274–279.
29. M. Fan, Z. Wang, H. Wu, W. Sun, and L. Zhang, "Low-threshold, high-efficiency random fiber laser with linear output," *IEEE Photonics Technol. Lett.* **27**(3), 319–322 (2015).
30. H. Wu, Z. Wang, M. Fan, L. Zhang, W. Zhang, and Y. Rao, "Role of the mirror's reflectivity in forward-pumped random fiber laser," *Opt. Express* **23**(2), 1421 (2015).